

Imaging Dirac Fermions Flow Through a Circular Veselago Lens

B. Brun¹, N. Moreau¹, S. Somanchi², V.-H. Nguyen¹, K. Watanabe³,

T. Taniguchi³, J.-C. Charlier¹, C. Stampfer² & B. Hackens¹

¹*IMCN/NAPS, Université catholique de Louvain (UCLouvain), B-1348 Louvain-la-Neuve, Belgium*

²*JARA-FIT and 2nd Institute of Physics - RWTH Aachen, Germany*

³*National Institute for Materials Science, Namiki, Tsukuba, Japan*

(Dated: June 20, 2019)

Graphene charge carriers behave as relativistic massless fermions, thereby exhibiting a variety of counter-intuitive behaviors. In particular, at p-n junctions, they behave as photons encountering a negative index media, therefore experiencing a peculiar refraction known as Veselago lensing. However, the way Dirac fermions flow through a Veselago lens remains largely unexplored experimentally. Here, a novel approach to create a movable and tunable circular p-n junction in graphene is proposed, using the polarized tip of a scanning gate microscope. Scanning the tip in the vicinity of a graphene constriction while recording the device conductance yields images related to the electron flow through a circular Veselago lens, revealing a high current density in the lens core, as well as two low current density zones along transport axis. Tight-binding simulations reveal the crucial role of the p-n junction smoothness on these phenomena. The present research adds new dimensions in the control and understanding of Dirac fermions optical elements, a prerequisite to engineer relativistic electron optics devices.

Optic-like manipulation of electron beams could in principle be achieved in p-n junctions, provided that the junction transmission is near perfect. However, in most cases, in particular in semiconductors, conventional p-n junctions are poor electron transmitters due to the inherent depletion of carriers in the vicinity of the junction. The discovery of graphene [1] changed this paradigm. Since charge carriers in graphene behave as massless Dirac fermions, Klein-like tunneling [2, 3] is at play, allowing perfect transmission for charge carriers impinging on a p-n junction perpendicularly. In addition, a diverging flow of Dirac fermions is refocused at a p-n interface, an effect known as Veselago lensing [4].

Using this negative refraction, invisibility cloak has been realized for microwave photons [5], and perfect electromagnetic lenses have been proposed [6]. The possibility of forming such Veselago lenses using p-n junctions in graphene [7, 8] as well as the resulting caustics [9–15] have attracted a lot of attention from a theoretical point of view. Recent works suggested that Veselago lensing could be used to create highly focused electron beams [16], and even a two-dimensional scanning Dirac fermions microscope [17]. But the experimental challenges required to materialize these visionary ideas have not yet been overcome. Though few experiments reported signatures of Veselago lensing [18, 19], the lack of tunability of such devices kept these discoveries to the state of “proof of concept”. The use of a scanning tunneling microscopy (STM) tip to induce circular p-n junctions and probe the resulting local density of states unveiled beautiful phenomena such as whispering gallery modes [20, 21] and quasi-bound states [22]. However, though these approaches reveal the rich internal electronic structure of p-n nano-islands, they cannot probe the current density *through* these p-n junctions and in their vicinity, an

essential parameter to control when designing Veselago-lensing-based devices.

In the present letter, a novel way to image current density through a tunable circular p-n junction, using a scanning gate microscope, is proposed. Scanning gate microscopy (SGM) consists in scanning a polarized metallic tip, acting as a local gate above a device’s surface, and mapping out tip-induced conductance changes [23]. Initially developed to investigate transport in III-V semiconductor heterostructures [24–26], it has been extended by several groups to investigate transport in graphene devices [27–33]. However, very few SGM experiments have been conducted yet on clean encapsulated graphene devices. Hence, it has proven difficult to observe electron-optics behavior in graphene using SGM, despite several theoretical predictions [34–36].

Here, the polarized SGM tip is used to create a movable and tunable circular Veselago lens. Applying a large voltage on the conductive tip induces circular p-n junction, whose potential can be controlled in amplitude and decay length. The tip scans in the vicinity of a constriction etched in a high mobility encapsulated graphene flake. Mapping the device conductance as a function of tip position yields images related to the electron flow through this Veselago lens. Surprisingly, transmission efficiency is drastically reduced when placing the lens next to the constriction entrances, and significantly enhanced when placing the lens at the constriction center. Tight-binding simulations indicate that SGM images partly reflect the current density distribution around the Veselago lens. The present work also emphasizes the role of the p-n interfaces sharpness and opens a door towards high precision optical elements design for Dirac fermions optics.

The sample consists of a single layer graphene flake

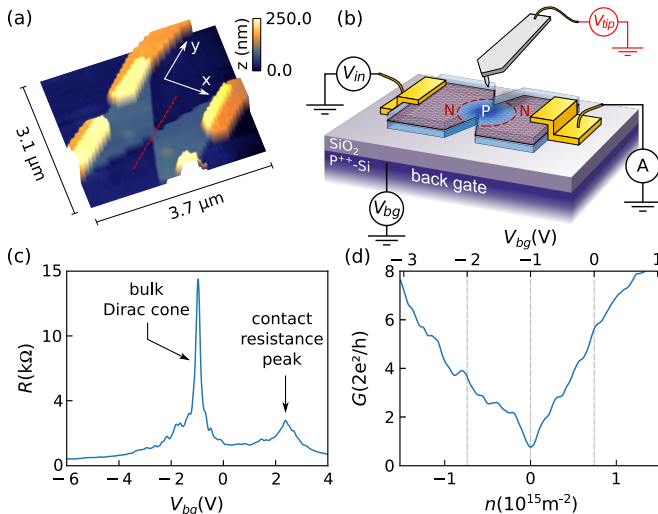


FIG. 1. **Graphene constriction:** (a) AFM image of the studied device (b) Scheme of the experiment: the charged AFM tip locally creates a n-p-n junction in the graphene flake. (c) Resistance as a function of backgate-voltage V_{bg} recorded in 2 contacts by standard lock-in technique at 4K, using an AC excitation of $35 \mu\text{V}$ at 77 Hz . The main Dirac cone is at a gate voltage of $V_{bg} = -1 \text{ V}$, and a smaller Dirac cone around $V_{bg} = +2.5 \text{ V}$ is due to one of the ohmic contacts. (d) Conductance as a function of V_{bg} around the main Dirac cone.

encapsulated between two 20 nm-thick h-BN flakes, deposited on top of a doped Si substrate covered by a 300 nm-thick SiO_2 layer. A 250 nm-wide constriction is defined by etching [37] (see Fig. 1a). The mean free path is of the order of the contacts separation (see supplemental materials [38]).

The sample is thermally anchored to the mixing chamber of a dilution refrigerator in front of a cryogenic scanning probe microscope [39]. Most of the data presented here are recorded at a temperature of 4 K, except Fig. 3(d-f) recorded at a base temperature of 28 mK. The conductance G of the device is measured between two line-contacts (as shown in Fig. 1b), and contact series resistances of 2 k Ω are taken into account. One of the contacts' resistance exhibits a strong dependence on back-gate voltage V_{bg} , and presents a secondary resistance peak around $V_{bg} = +2.5 \text{ V}$ (Fig. 1c). Note that this does not play any role here since the absolute G value is not discussed, only its relative variations.

We now discuss transport under the influence of the scanning tip. The biased tip locally changes the carriers density n , in an isotropic way, leading to a Lorentzian evolution of n , centered at the tip position. When a p-n junction is induced by the biased tip, this Lorentzian profile sharpness has a crucial influence on Dirac fermion semi-classical trajectories in its vicinity [40]. It is therefore important to extract this profile from our experimental data. For this, we scan the tip along a line per-

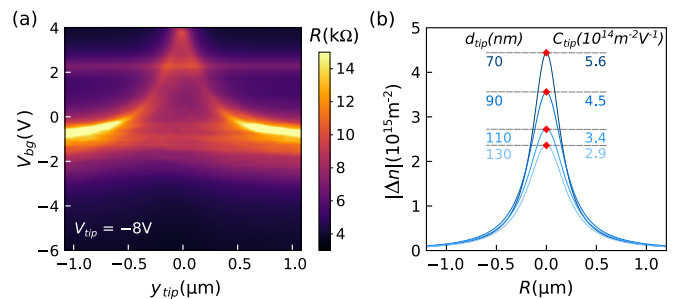


FIG. 2. **Evaluation of the tip-induced potential:** (a) Resistance as a function of tip position along red dashed line Fig. 1a (zero being the center of the constriction), and V_{bg} . $d_{tip} = 90 \text{ nm}$, $V_{tip} = -8 \text{ V}$. (b) Tip lever-arm parameter evolution with d_{tip} , for $V_{tip} = -8 \text{ V}$

pendicular to the constriction transport axis (red dashed line in Fig. 1a and 3a), at a distance d_{tip} from the sample surface, and map the device resistance R as a function of back-gate voltage (Fig. 2a). The locus of maxima in the line profile mapping as a function of V_{bg} draws a Lorentzian shape centered at the constriction. This locus corresponds to the tip-position-dependent value of V_{bg} required to locally reach the Dirac point at the center of the constriction, hence the change in n required to compensate the tip-induced local change of density. In other words, the Lorentzian shape in Fig. 2a directly maps the effect of the tip-induced potential on the local carrier density, provided that the V_{bg} -axis is properly scaled into the local carrier density change Δn . The Lorentzian maximum linearly scales with tip voltage V_{tip} , allowing its characterization by a simple lever-arm parameter that depends on tip-to-graphene distance d_{tip} , as shown Fig. 2b. The half width at half maximum R_{tip} depends also on V_{tip} and d_{tip} and varies between 200 and 300 nm (see supplemental materials).

With this fully-characterized tip influence, the SGM images (i.e. conductance as a function of tip position) can be analyzed. They are obtained by scanning the tip above the sample at fixed V_{tip} and V_{bg} . Figure 3 shows such SGM maps, in different conditions of bulk carrier densities, tip voltages and temperature T . Figure 3a-c shows the evolution of the SGM contrast with carrier density. V_{bg} is chosen such that bulk transport is governed by electrons. In Fig. 3a, the highest tip-induced density change ($\Delta n_{max} \sim -2.3 \times 10^{15} \text{ m}^{-2}$) is lower than the bulk electron density ($3 \times 10^{15} \text{ m}^{-2}$). This therefore corresponds to a n-n'-n configuration, inducing a quasi-isotropic decrease of G as the negatively-biased tip moves away from the constriction center. This means that G is governed by the constriction region, and that reducing the carriers density in the center of the constriction reduces the total transmission, as naturally expected. This prominent influence of the constriction on transport justifies the validity of the above-described method to char-

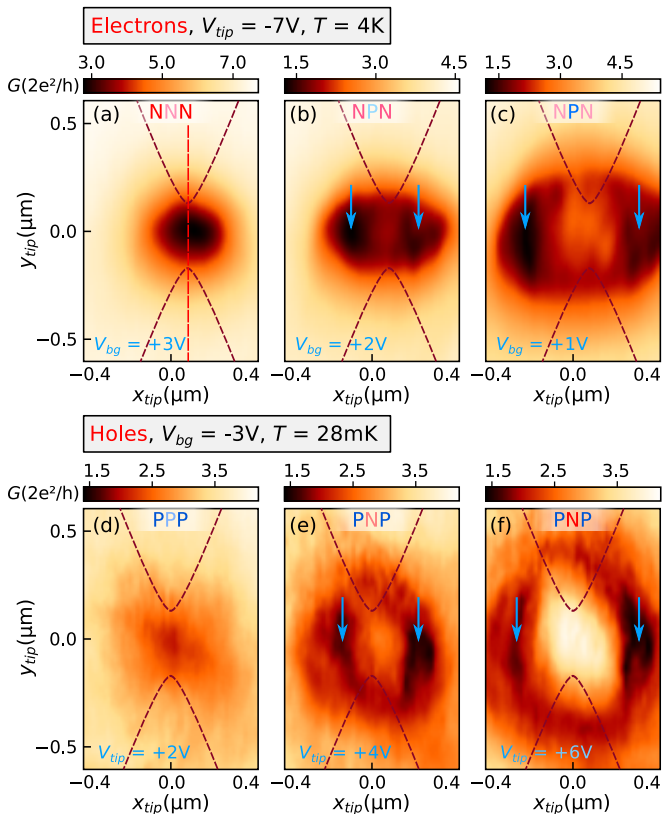


FIG. 3. **SGM images evolution with carrier density and temperature:** (a) to (c) SGM images on electron side at 4K, for $V_{tip} = -7$ V and $d_{tip} = 120$ nm, inducing a density change $\Delta n_{max} \sim -2.3 \times 10^{15} \text{ m}^{-2}$. (a) Bulk density $n = 3 \times 10^{15} \text{ m}^{-2}$; (b) $2.2 \times 10^{15} \text{ m}^{-2}$; (c) $1.5 \times 10^{15} \text{ m}^{-2}$. (d) to (f): SGM images at 28 mK on holes side for $n = -1.5 \times 10^{15} \text{ m}^{-2}$ and $d_{tip} = 120$ nm for different V_{tip} corresponding to $\Delta n_{max} =$ (d) $1.2 \times 10^{15} \text{ m}^{-2}$; (e) $2.5 \times 10^{15} \text{ m}^{-2}$; (f) $3.7 \times 10^{15} \text{ m}^{-2}$.

acterize the tip-induced potential. For lower bulk densities (Fig. 3b-c), the tip bias creates a circular n-p-n junction. In this case, an important qualitative change is observed. Contrary to Fig. 3a, we observe a local maximum of G when the tip is placed at the very center of the constriction, surrounded by an elliptic region of reduced conductance. Interestingly, G change is not isotropic anymore, and two spots of lower G are clearly visible on both sides of the constriction, as indicated by arrows in Fig. 3b-c.

A similar behavior is observed for hole-type carriers, as shown in Fig. 3d-f. Here, the bulk hole density is fixed ($V_{bg} = -3$ V) and V_{tip} is varied. Once again, reducing the hole density below the tip leads to a quasi-isotropic single spot of reduced G (Fig. 3d). But if V_{tip} is chosen such that it locally changes the charge carriers sign (i.e. a circular p-n-p region is created), a local maximum of G is observed when placing the tip at the very center of the constriction, and two regions of lower G are visible when placing the tip on both sides of the constriction along

transport axis (Fig. 3e-f). Note that data in Fig. 3d-f are recorded at $T = 28$ mK, which does not qualitatively change the main observations compared to Fig. 3a-c, recorded at 4 K. Noteworthy, the main features are really robust to temperature changes, and still observable up to 100 K (see supplemental materials).

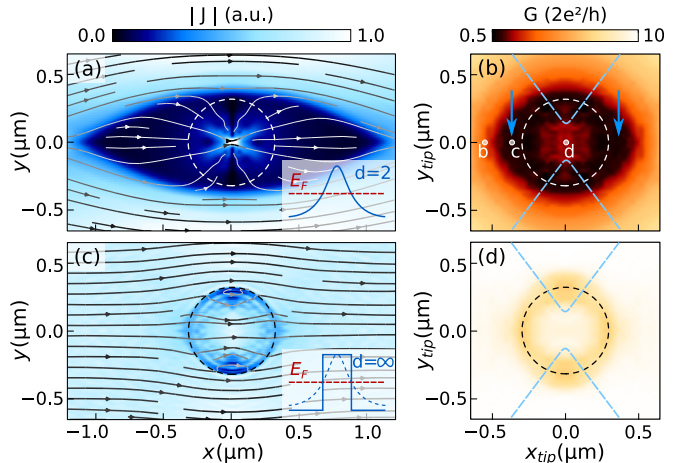


FIG. 4. **Tight-binding simulations:** Simulations of current density \mathbf{J} in a graphene sheet around the fixed tip potential of Eq. (1) characterized by the parameters V_m , E and d (left image in each couple), and simulated SGM maps obtained by displacing the same potential around a 250 nm-wide constriction (right image in the couple). (a-b) n-p-n configuration with $d = 2$ and $V_m = 2E$. (c-d) Abrupt circular p-n junction with $d = \infty$ and $V_m = 2E$. The chosen energy E corresponds in all cases to $n = 1.5 \times 10^{15} \text{ m}^{-2}$, and $\Delta n_{max} = -3 \times 10^{15} \text{ m}^{-2}$. Dashed circle indicates the locus corresponding to zero charge density. Insets: schematics of potential profile vs position.

In the following, we discuss the origin of the observed features, and evidence a correspondence between the SGM maps and the current density pattern inside and around a tip-induced circular Veselago lens. It should first be stressed that a model of the experiment assuming diffusive transport in the constriction region cannot reproduce our observations (see section V of the supplemental materials [38]). The measured mobility is limited by the ohmic contacts separation, indicating ballistic transport on a scale larger than the radius of the circular p-n junction defined by the tip. This is corroborated by the observation of Fabry-Pérot interference in the n-p-n and p-n-p configurations [41].

To understand the contrast in SGM images, tight-binding simulations of transport through model graphene devices are performed, using a home-made recursive Green function code [42]. The charge carrier flow around a tip-induced potential is first investigated in an infinite graphene sheet without the constriction, as shown in Fig. 4 a and c. The tip-induced perturbation is included by

imposing a potential

$$V(\mathbf{r}) = \frac{V_m}{1 + \left(\frac{\|\mathbf{r} - \mathbf{r}_{tip}\|}{R_{tip}} \right)^d} \quad (1)$$

where \mathbf{r}_{tip} is the tip position, R_{tip} the potential decay length and d the decay exponent. The current density $|\mathbf{J}|$ is computed at a given energy E . Note that all distances, energies and potential are scaled to match the experimental parameters. Figure 4a presents the current density around a Lorentzian potential ($d=2$ in Eq.(1)) fixed at $\mathbf{r}_{tip} = (0, 0)$, for $R_{tip} = 300$ nm and $V_m = 2E$, therefore inducing a circular p-n junction. In this configuration, $|\mathbf{J}|$ is maximal at the center of the junction. Figure 4b shows the computed SGM map when the perturbation is scanned around a 250 nm-wide constriction (represented by blue dashed lines), i.e. the system transmission as a function of the Lorentzian potential position.

These tight-binding simulations capture the essential features observed in the experimental SGM images (Fig. 3), and the comparison with current density maps shines light on the mechanisms at play in the experiment. Indeed, scanning the tip in the vicinity of a constriction yields SGM images that are qualitatively similar to the current density pattern around and through the tip-induced circular p-n junction. This result contrasts with SGM images obtained on GaAs quantum point contacts, which take advantage of the tip-induced backscattering to image the unperturbed electron wavefunctions [43], or trajectories through the bulk disordered potential [24, 44]. In graphene, backscattering is prevented by pseudo-spin conservation [40], leading to Klein tunneling, and this reverses the paradigm of SGM experiment. In turn, this allows to study the Dirac fermion flow through the tip potential.

Klein tunneling is characterized by a perfect transmission for trajectories impinging perpendicularly to a p-n junction. Beside this effects, trajectories crossing the junction at finite angles are refracted with a negative index. Given the circular geometry in our experiment, which offers a large collection of incidence angle, these two manifestations of the same physical phenomenon do contribute to the high $|\mathbf{J}|$ spot at the p-n junction center.

The smoothness of the p-n interface strongly impacts the transmission probability at finite incident angle [19, 40, 45, 46]. For equal carrier densities in the p and n regions, this probability for an incidence angle ϕ is given by $T(\phi) = e^{-\pi k_F \omega \sin^2(\phi)}$, where k_F is the Fermi wavevector, and ω the junction width. This indicates that trajectories impinging with an incident angle up to $\sim 20^\circ$ are refracted with a negative index and contribute to the total transmission in our experimental conditions.

The SGM images reveal two main features of the charge flow through the p-n junction: (i) The local maximum of transmission, observed when the tip is placed at the center of the constriction, reflects the high current

density at the lens core in the n-p-n or p-n-p configuration. (ii) The reduced conductance spots observed when the tip is placed slightly away from the constriction, indicated by arrows in Fig. 4b and very similar to the experimentally observed spots in Fig. 3, are the *loci* of all the tip positions for which the transmission of Dirac fermions through the constriction is strongly reduced. This is reminiscent of the effect visible in Fig. 4a where the tip also induces low current density (dark) regions on the sides of the tip-induced p-n junction.

Interestingly, the smoothness of the p-n junctions plays a crucial role in the emergence of the low conductance and low $|\mathbf{J}|$ points. They are due to the smooth electrostatic potential evolution that bends electron trajectories away from the lens, as would photons in a gradient index medium. They almost vanish and match the *loci* of zero charge density in the case of an infinitely sharp circular potential, as shown in Fig. 4c for the current density, and concomitantly in Fig. 4d for the calculated SGM map.

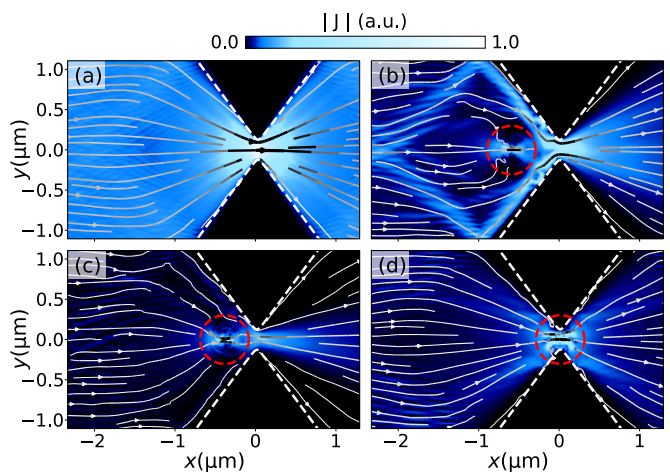


FIG. 5. **Distortion of the flow by the constriction:** (a) Current density through the constriction without tip potential. (b-d) Current density through the tip and the constriction for different tip-to-constriction distances, indicated in Fig.4b. The tip potential is the same as in Fig.4a-b.

Noteworthy, the patterns observed in the SGM maps in the case of a smooth junction are significantly distorted with respect to the corresponding current density patterns. For example, the distance from the reduced conductance spot to the constriction center in Fig. 4b is different than the distance from the lowest current density to the lens center in Fig. 4a. The spot of enhanced conductance also appears wider than the sharp spot of high current density. The constriction shape plays a central role in this distortion, as it alters Dirac fermions trajectories. The finite opening angle of the etched region causes a focusing of current density lines towards the constriction, as depicted in Fig.5a where we plot the current density \mathbf{J} through the constriction. When the tip is over the position of minimum $|\mathbf{J}|$ along transport

axis (position b in Fig.4b), the total transmission is still high because of trajectories refocused by the constriction edges, as evidenced in Fig.5b. The lowest total transmission is obtained when the tip also blocks these trajectories, as depicted in Fig.5c. Finally, when placing the tip at the center of the constriction, current density lines are perpendicular to the p-n interface (Fig. 5b) and the efficient Klein tunneling in this configuration leads to a high transmission. Noticeably, in the case of an abrupt constriction, the simulated SGM images appear more similar to the current density patterns around the Veselago lens than in the current geometry (with V-shaped etched regions), which offers promising perspectives for future experiments (See Fig.S9 [38]).

In conclusion, a SGM tip scanned above a high mobility graphene device is used to create a smooth circular Veselago lens. By scanning the tip in the vicinity of a constriction, images related to the electron flow through this circular p-n junction are obtained, as confirmed by tight-binding simulations. In particular, a high current density is observed at the lens core, as a direct consequence of Klein tunneling. The present study also reveals the existence of low current density points away from a smooth circular p-n junction, highly sensitive to the junction smoothness. While many studies investigated caustics of Veselago lenses [9–15] (i.e. points at which trajectories density diverges), the existence of such low current density points may prove very useful in the future design of Dirac fermions optical elements, adding a new possibility to the existing toolbox.

The present research was funded by the Fédération Wallonie-Bruxelles through the ARC Grant on 3D nanoarchitecturing of 2D crystals (No. 16/21-077) and from the European Union's Horizon 2020 Research and Innovation program (No. 696656). B.B. (research assistant), N.M. (FRIA fellowship), B.H. (research associate), V.-H.N. and J.-C.C. (PDR No. T.1077.15) acknowledge financial support from the F.R.S.-FNRS of Belgium. Support by the Helmholtz Nanoelectronic Facility (HNF), the EU ITN SPINOGRAPH and the DFG (SPP-1459) is gratefully acknowledged. Growth of hexagonal boron nitride crystals was supported by the Elemental Strategy Initiative conducted by the MEXT, Japan and JSPS KAKENHI Grant Numbers JP26248061, JP15K21722 and JP25106006. B.H. thanks Z. Zanolli for the connection with C.S. B.B acknowledges the use of Kwant [47] used to guide the experiment and cross-check tight-binding simulations.

[1] K. S. Novoselov, A. K. Geim, S. V. Morozov, D. Jiang, M. I. Katsnelson, I. V. Grigorieva, S. V. Dubonos, and A. A. Firsov, *Nature* **438**, 197 (2005).
 [2] O. Klein, *Zeitschrift für Physik* **53**, 157 (1929).
 [3] A. F. Young and P. Kim, *Nature Physics* **5**, 222 (2009).

[4] V. G. Veselago, *Soviet Physics Uspekhi* **10**, 509 (1968).
 [5] D. Schurig, J. J. Mock, B. J. Justice, S. A. Cummer, J. B. Pendry, A. F. Starr, and D. R. Smith, *Science* **314**, 977 (2006).
 [6] J. B. Pendry, *Phys. Rev. Lett.* **85**, 3966 (2000).
 [7] V. V. Cheianov, V. Fal'ko, and B. L. Altshuler, *Science* **315**, 1252 (2007).
 [8] S. P. Milovanovi, D. Moldovan, and F. M. Peeters, *Journal of Applied Physics* **118**, 154308 (2015).
 [9] J. Cserti, A. Pályi, and C. Péterfalvi, *Phys. Rev. Lett.* **99**, 246801 (2007).
 [10] W. Mu, G. Zhang, Y. Tang, W. Wang, and Z. Ou-Yang, *Journal of Physics: Condensed Matter* **23**, 495302 (2011).
 [11] N. A. Garg, S. Ghosh, and M. Sharma, *Journal of Physics: Condensed Matter* **26**, 155301 (2014).
 [12] J.-S. Wu and M. M. Fogler, *Phys. Rev. B* **90**, 235402 (2014).
 [13] R. Logemann, K. J. A. Reijnders, T. Tudorovskiy, M. I. Katsnelson, and S. Yuan, *Phys. Rev. B* **91**, 045420 (2015).
 [14] M. Lu and X.-X. Zhang, *Journal of Physics: Condensed Matter* **30**, 215303 (2018).
 [15] S.-H. Zhang, W. Yang, and F. M. Peeters, *Phys. Rev. B* **97**, 205437 (2018).
 [16] M.-H. Liu, C. Gorini, and K. Richter, *Phys. Rev. Lett.* **118**, 066801 (2017).
 [17] P. Bøggild, J. M. Caridad, C. Stampfer, G. Calogero, N. R. Papior, and M. Brandbyge, *Nature Communications* **8**, 15783 (2017), article.
 [18] G.-H. Lee, G.-H. Park, and H.-J. Lee, *Nature Physics* **11**, 925 (2015).
 [19] S. Chen, Z. Han, M. M. Elahi, K. M. M. Habib, L. Wang, B. Wen, Y. Gao, T. Taniguchi, K. Watanabe, J. Hone, A. W. Ghosh, and C. R. Dean, *Science* **353**, 1522 (2016).
 [20] Y. Zhao, J. Wyrick, F. D. Natterer, J. F. Rodriguez-Nieva, C. Lewandowski, K. Watanabe, T. Taniguchi, L. S. Levitov, N. B. Zhitenev, and J. A. Stroscio, *Science* **348**, 672 (2015).
 [21] Y. Jiang, J. Mao, D. Moldovan, M. R. Masir, G. Li, K. Watanabe, T. Taniguchi, F. M. Peeters, and E. Y. Andrei, *Nature Nanotechnology* **12**, 1045 (2017).
 [22] J. Lee, D. Wong, J. Velasco Jr, J. F. Rodriguez-Nieva, S. Kahn, H.-Z. Tsai, T. Taniguchi, K. Watanabe, A. Zettl, F. Wang, L. S. Levitov, and M. F. Crommie, *Nature Physics* **12**, 1032 (2016).
 [23] M. A. Eriksson, R. G. Beck, M. Topinka, J. A. Katine, R. M. Westervelt, K. L. Campman, and A. C. Gossard, *Applied Physics Letters* **69**, 671 (1996), →.
 [24] M. A. Topinka, B. J. LeRoy, R. M. Westervelt, S. E. J. Shaw, R. Fleischmann, E. J. Heller, K. D. Maranowski, and A. C. Gossard, *Nature* **410**, 183 (2001).
 [25] M. P. Jura, M. A. Topinka, M. Grobis, L. N. Pfeiffer, K. W. West, and D. Goldhaber-Gordon, *Phys. Rev. B* **80**, 041303(R) (2009).
 [26] A. A. Kozikov, C. Rössler, T. Ihn, K. Ensslin, C. Reichl, and W. Wegscheider, *New Journal of Physics* **15**, 013056 (2013).
 [27] S. Schnez, J. Güttinger, M. Huefner, C. Stampfer, K. Ensslin, and T. Ihn, *Phys. Rev. B* **82**, 165445 (2010).
 [28] N. Pascher, D. Bischoff, T. Ihn, and K. Ensslin, *Applied Physics Letters* **101**, 063101 (2012).
 [29] A. G. F. Garcia, M. König, D. Goldhaber-Gordon, and K. Todd, *Phys. Rev. B* **87**, 085446 (2013).
 [30] D. Cabosart, A. Felten, N. Reckinger, A. Iordanescu,

- S. Toussaint, S. Faniel, and B. Hackens, *Nano Letters* **17**, 1344 (2017).
- [31] S. Bhandari, G.-H. Lee, A. Klales, K. Watanabe, T. Taniguchi, E. Heller, P. Kim, and R. M. Westervelt, *Nano Letters* **16**, 1690 (2016).
- [32] Z. Dou, S. Morikawa, A. Cresti, S.-W. Wang, C. G. Smith, C. Melios, O. Kazakova, K. Watanabe, T. Taniguchi, S. Masubuchi, T. Machida, and M. R. Connolly, *Nano Letters* **18**, 2530 (2018).
- [33] S. Xiang, A. Mreńca-Kolasińska, V. Miseikis, S. Guiducci, K. Kolasiński, C. Coletti, B. Szafran, F. Beltram, S. Roddaro, and S. Heun, *Phys. Rev. B* **94**, 155446 (2016).
- [34] A. Mreca, K. Kolasinski, and B. Szafran, *Semiconductor Science and Technology* **30**, 085003 (2015).
- [35] A. Mreńca-Kolasińska, S. Heun, and B. Szafran, *Phys. Rev. B* **93**, 125411 (2016).
- [36] A. Mreńca-Kolasińska and B. Szafran, *Phys. Rev. B* **96**, 165310 (2017).
- [37] B. Terrés, L. A. Chizhova, F. Libisch, J. Peiro, D. Jörgen, S. Engels, A. Girschik, K. Watanabe, T. Taniguchi, S. V. Rotkin, J. Burgdröfer, and C. Stampfer, *Nature Communications* **7**, 11528 (2016), article.
- [38] *See supplemental materials for additional data and analysis, which also includes Refs.[48–52].*
- [39] B. Hackens, F. Martins, S. Faniel, C. A. Dutu, H. Sellier, S. Huant, M. Pala, L. Desplanque, X. Wallart, and V. Bayot, *Nat. Commun.* **1**, 39 (2010).
- [40] P. E. Allain and J. N. Fuchs, *The European Physical Journal B* **83**, 301 (2011).
- [41] *At low temperature, we observe Fabry-Pérot oscillations in n-p-n an p-n-p configuration when placing the tip at the center of the constriction (see section XI of the supplemental materials [38]).*
- [42] V. H. Nguyen, A. Bournel, and P. Dollfus, *Journal of Physics: Condensed Matter* **22**, 115304 (2010).
- [43] M. A. Topinka, B. J. LeRoy, S. E. J. Shaw, E. J. Heller, R. M. Westervelt, K. D. Maranowski, and A. C. Gossard, *Science* **289**, 2323 (2000).
- [44] B. A. Braem, C. Gold, S. Hennel, M. Rslı, M. Berl, W. Dietsche, W. Wegscheider, K. Ensslin, and T. Ihn, *New Journal of Physics* **20**, 073015 (2018).
- [45] V. V. Cheianov and V. I. Fal'ko, *Phys. Rev. B* **74**, 041403(R) (2006).
- [46] F. Libisch, T. Hisch, R. Glattauer, L. A. Chizhova, and J. Burgdröfer, *Journal of Physics: Condensed Matter* **29**, 114002 (2017).
- [47] C. W. Groth, M. Wimmer, A. R. Akhmerov, and X. Waintal, *New Journal of Physics* **16**, 063065 (2014).
- [48] K. K. Kim, A. Hsu, X. Jia, S. M. Kim, Y. Shi, M. Dresselhaus, T. Palacios, and J. Kong, *ACS Nano* **6**, 8583 (2012), <https://doi.org/10.1021/nn301675f>.
- [49] V. Hung Nguyen, J. Saint-Martin, D. Querlioz, F. Mazzamuto, A. Bournel, Y.-M. Niquet, and P. Dollfus, *Journal of Computational Electronics* **12**, 85 (2013).
- [50] A. H. Castro Neto, F. Guinea, N. M. R. Peres, K. S. Novoselov, and A. K. Geim, *Rev. Mod. Phys.* **81**, 109 (2009).
- [51] C. H. Lewenkopf and E. R. Mucciolo, *Journal of Computational Electronics* **12**, 203 (2013).
- [52] M.-H. Liu, P. Rickhaus, P. Makk, E. Tóvári, R. Maurand, F. Tkatschenko, M. Weiss, C. Schönenberger, and K. Richter, *Phys. Rev. Lett.* **114**, 036601 (2015).

Imaging Dirac Fermions Flow Through a Circular Veselago Lens - Supplemental materials -

B. Brun¹, N. Moreau¹, S. Somanchi², V.-H. Nguyen¹, K. Watanabe³,
T. Taniguchi³, J.-C. Charlier¹, C. Stampfer² & B. Hackens¹

¹IMCN/NAPS, Université catholique de Louvain (UCLouvain), B-1348 Louvain-la-Neuve, Belgium

²JARA-FIT and 2nd Institute of Physics - RWTH Aachen, Germany

³National Institute for Materials Science, Namiki, Japan

June 19, 2019

1 Determination of the lever-arm

In order to convert the back gate voltage V_{bg} into a charge carrier density n_{2D} , we need to evaluate the lever arm defined by $C = n/\Delta V$ where $\Delta V = V_{bg} - V_{CNP}$ with $V_{CNP} = -1$ V in our sample. This can be achieved by two different methods:

- From a simple capacitor model with $d_{h-BN} = 30$ nm and $d_{SiO_2} = 300$ nm, the lever-arm is $C = 6.1 - 6.7 \times 10^{14} \text{m}^{-2}\text{V}^{-1}$, depending on h-BN dielectric constant ($\epsilon_{h-BN} = 2 - 4$) [1].
- From Shubnikov-de Haas (SdH) oscillations, the Landau levels positions in the (V_g, B) plane are given by the expression

$$B_\nu = \frac{\pi\hbar}{2e\nu} C \Delta V$$

where ν is the filling factor. By fitting the Landau levels positions in the conductance map in the (V_g, B) plane (Fig. S1b), measured in the bulk of the sample (see Fig. S1a for the measurement configuration), we obtain $C = 7.4 \pm 0.2 \times 10^{14} \text{m}^{-2}\text{V}^{-1}$.

2 Mobilities

Charge carriers mobilities are extracted from linear fits to the G vs n curve in the vicinity of the charge neutrality point (i.e. the Dirac cone). Note that we measure G in the two-contacts configuration depicted in Fig. S1a, taking into account a total series resistance of 2 k Ω corresponding to the electrical filters on the measurement setup. This yields lower bounds for the mobilities : $\mu_e \sim 40\,000 \text{cm}^2\text{V}^{-1}\text{s}^{-1}$ for electrons and $\mu_h \sim 28\,000 \text{cm}^2\text{V}^{-1}\text{s}^{-1}$ for holes.

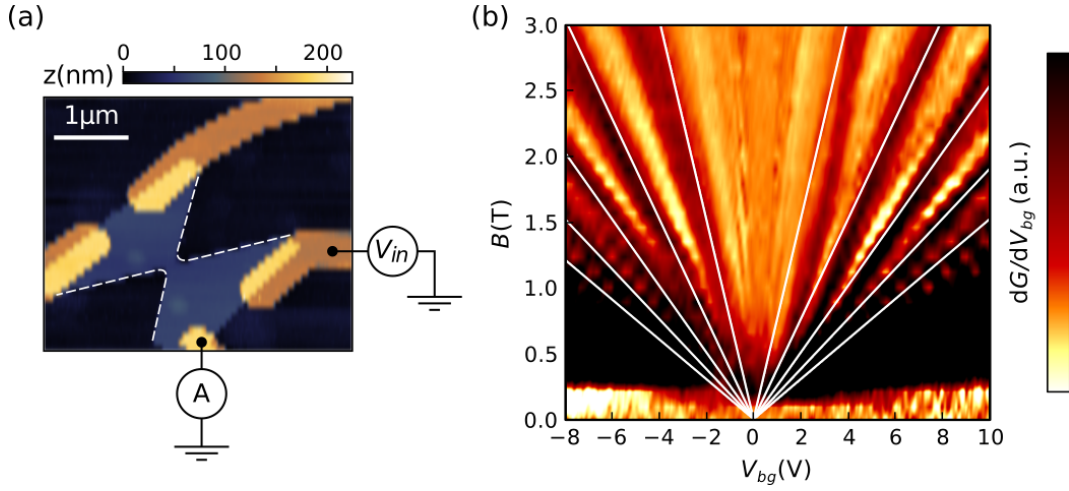


Figure S1: Lever-arm parameter of the back-gate. (a) AFM topography image of the graphene device. The two contacts used for the transconductance measurement shown in (b) are below the constriction, in yellow, and separated from each other by a distance of 800 nm. (b) Transconductance $\partial G/\partial V_{bg}$ as a function of V_{bg} and B .

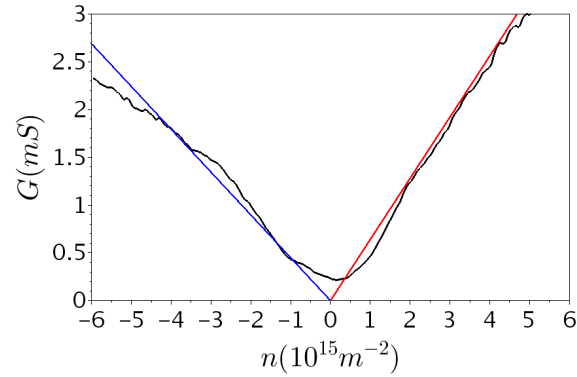


Figure S2: Electron and holes mobilities from the Dirac cone slope. Dirac cone measured in the same configuration as Fig. S1a. Two linear fits allow to calculate lower bounds for the electron and holes mobilities.

3 Temperature robustness

The main features of the SGM images discussed in the main text are visible at a temperature of ≈ 100 K. Fig. S3 shows SGM maps for a tip voltage of -8 V and a tip-to-graphene distance of

≈ 100 nm. The vertical as well as the horizontal length scales are only roughly estimated since we have no calibration for our piezoelectric scanner at 100 K. These images therefore just bring a qualitative insight on the temperature robustness of the observed features.

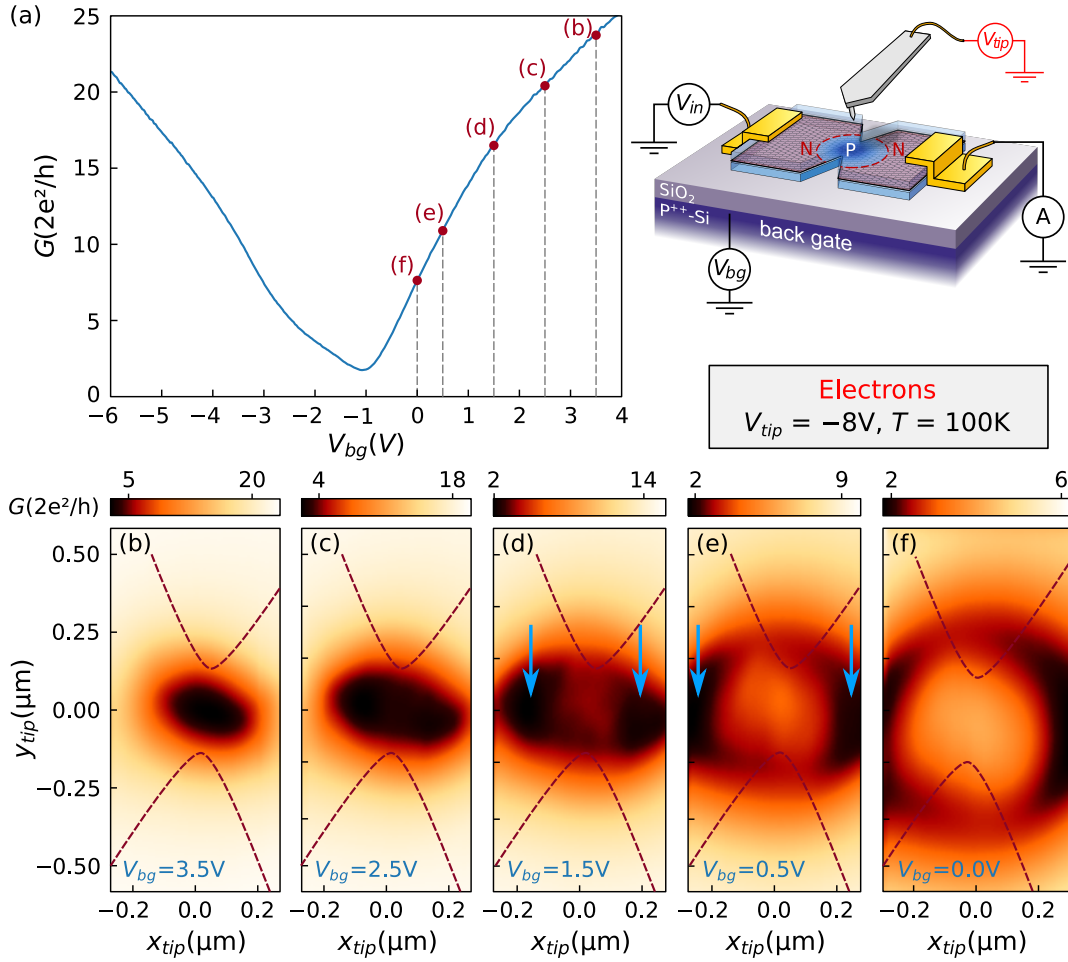


Figure S3: Signatures of Veselago lensing at high temperature. (a) G vs V_{bg} across the QPC, measured in four-contacts configuration, at a temperature around 100 K. (b-f) SGM maps for a tip voltage -8 V and tip-to-graphene distance of ≈ 100 nm, for the gate voltages indicated on (a).

4 Tip characterization

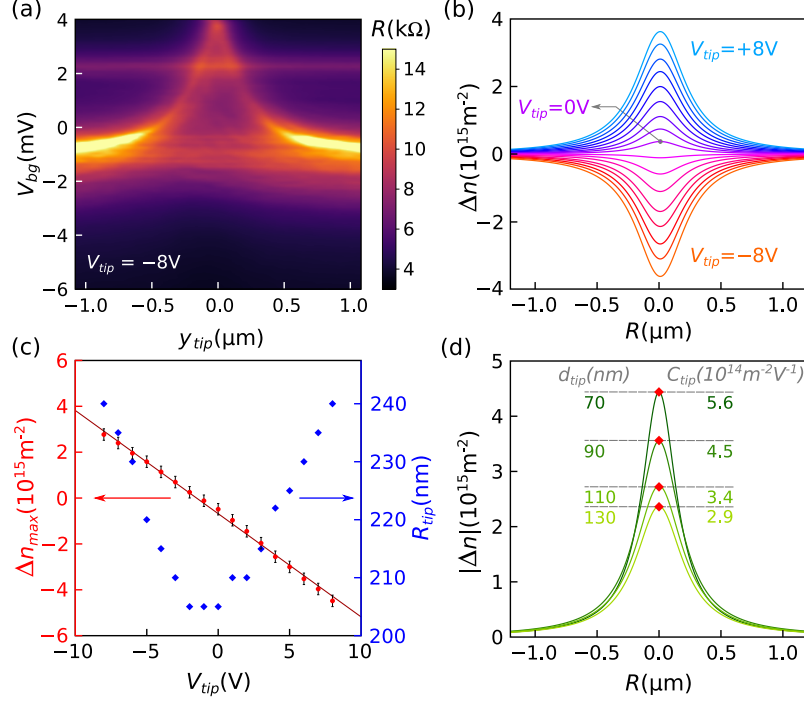


Figure S4: Evaluation of the tip-induced potential. (a) Resistance map as a function of tip position along a line passing by the centre of the constriction (position 0.0) perpendicularly to the transport axis, and V_{bg} . $d_{tip} = 90$ nm, $V_{tip} = -8$ V. (b) Fits of the tip-induced resistance maxima as a function of tip position extracted for different values of V_{tip} , from -8 V to $+8$ V, and $d_{tip} = 90$ nm, converted into local carrier density. (c) Evaluation of maximum charge density change around the center of the tip-affected region as a function of tip voltage (red points), and linear fit giving a tip lever-arm $C_{tip} = 4,5 \times 10^{14} m^{-2} V^{-1}$ (red line). R_{tip} , corresponding to half-width at half maximum of the Lorentzian fits in (b), as a function of V_{tip} (blue dots). (d) Tip lever-arm parameter evolution with d_{tip} , for $V_{tip} = -8$ V

Fig. S4 presents the full characterization of the tip-induced potential for different tip voltages. As in the main text, we scan the tip along a line perpendicular to the QPC transport axis (red dashed line in Fig. 1a in the main text), and map the resistance R as a function of back-gate voltage. The resulting figure exhibits a Lorentzian-shape maximum, as shown in Fig. S4a.

Horizontal lines can also be noticed in Fig. S4a, around $V_{bg} = +2.3$ V and $V_{bg} = -1$ V. The one at $V_{bg} = +2.3$ V corresponds to the contribution of the series ohmic contact responsible for the second Dirac cone also visible at $V_{bg} = +2.3$ V in Fig. 1c of the manuscript. It is therefore completely insensitive to the tip position along this specific line since this contact is far away from the scan line. The horizontal conductance minimum around $V_{bg} = -1$ V corresponds to the bulk

Dirac cone, i.e. away from the constriction.

Acquiring mappings similar to Fig. S4a, for different tip voltages at a fixed tip-to-graphene distance of 90 nm, yields the set of Lorentzian fits to the data displayed Fig. S4b.

In figure S4c we summarize these fits by plotting the maximum density change on top of the Lorentzian Δn_{max} (red dots, right axis) and its half-width at half maximum R_{tip} (blue dots, left axis). The maximum tip-induced density change as a function of tip voltage scales almost linearly with tip voltage, which allows us to characterize it by a simple lever-arm parameter $C_{tip} = 4.5 \times 10^{14} \text{ m}^{-2}\text{V}^{-1}$ for this tip-to-graphene distance.

5 Ruling out diffusive transport

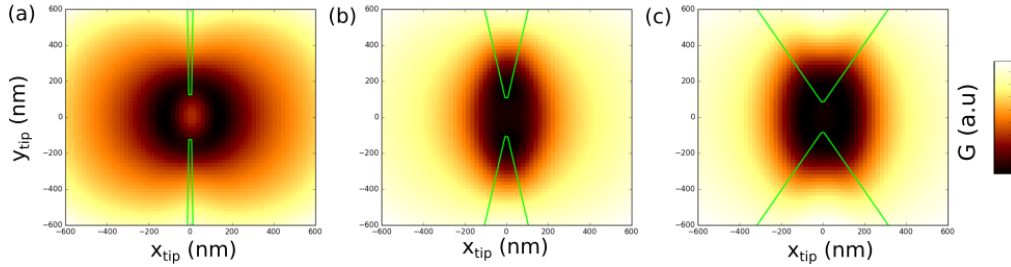


Figure S5: Diffusive model: (a) Total resistance calculated for a single opening dominating all the device resistance. The tip potential induces a change of carriers with a density change $\Delta n_{max} = -2 * n_{bulk}$. (b) Total resistance for a small opening angle constriction, with the same potential profile. (c) Total resistance for a constriction with a geometry corresponding to the experiment.

To check whereas diffusive transport could explain our observations, we study a simple one-dimensional model of the experiment, considering series resistance along the x -axis. Following early works on p-n junctions aiming at distinguishing between ballistic and diffusive transport [2], we assume a local conductivity $\sigma(x, y) = (\sigma_0^2 + [\mu en(x, y)]^2)^{1/2}$, where σ_0 is the residual conductivity at the charge neutrality point, n the local density, μ the mobility and e the electron charge. We then consider slices at abscissa x , that have a resistance $R(x)$ that depends on the density integrated over the y direction. The potential landscape is a Lorentzian similar to the one characterized in the manuscript, leading to a change in density $\Delta n_{max} = -2 * n_{bulk}$ at its maximum. The total conductance of the device is analyzed in this diffusive case, and plotted Fig.S5 as a function of tip position. FigS5a presents the case of a single aperture that would dominate the overall conductance of the device. In that case, a pattern that reminds the SGM maps observed experimentally is obtained, where the conductance when placing the tip at the center of the constriction is the same as when it is very far away. This is not surprising since the total resistance is given by the density at the constriction. However, considering the geometry of the experiment destroys this effect (Fig.S5c), because the openings of the constriction also contribute to the total resistance, and are affected by the tip too. The effect of the tip on the total transmission is more monotonic in that case, and the tip can only reduce the total transmission. This simple model shows that

diffusive transport alone cannot account for the observed behavior, and that ballistic trajectories and transmission and refraction laws at graphene p-n interfaces have to be taken into account.

6 Tight-binding simulations

In this section, we introduce briefly the tight-binding calculations [3] used to simulate the current density and the SGM maps presented in the main text (Fig. 4). Similar simulations have also been performed with the Kwant package [4] and led to the same conclusions.

The electronic properties of the considered graphene system are modeled by a first-nearest-neighbor tight-binding Hamiltonian [5]:

$$H = \sum_n V_n c_n^\dagger c_n + t \sum_{\langle n,m \rangle} c_n^\dagger c_m \quad (1)$$

where t represents the hopping energy between first-nearest-neighbor n^{th} and m^{th} atoms and V_n corresponds to the potential energy induced by gate voltages at the n^{th} site. To compute the transport quantities, this tight-binding Hamiltonian is solved using the Green's function technique [3]. In particular, the retarded Green's function is determined as:

$$\mathcal{G}(E) = [E + i0^+ - H - \Sigma_L - \Sigma_R]^{-1}, \quad (2)$$

where $\Sigma_{L,R}$ are the self-energies describing the left and right device-to-lead couplings, respectively. This Green's function equation is solved using the recursive method [6]. The transport quantities such as conductance and bond currents injected from the left lead are then computed using the following formulas:

$$G(E_F) = \frac{2e^2}{h} \text{Tr} [\Gamma_L \mathcal{G} \Gamma_R \mathcal{G}^\dagger], \quad (3)$$

$$J_{nm}^L(E_F) = -\frac{2e}{h} H_{nm} \text{Im} (\mathcal{G} \Gamma_L \mathcal{G}^\dagger)_{nm} \quad (4)$$

with $\Gamma_{L,R} = i (\Sigma_{L,R} - \Sigma_{L,R}^\dagger)$.

In order to simulate graphene devices of similar sizes (i.e., at the μm scale) as in the experiments, there is however a numerical challenge. In particular, the simulation of such large graphene system (typically, more than 8000 lattice sites in transverse direction for $W = 1 \mu\text{m}$) includes several million carbon orbitals. Hence, to avoid such numerical challenge, we employed the scaling technique as presented in [7], that has been demonstrated to work very well for graphene device simulations. In particular, we increase the bond length a_{CC} between the carbon atoms by a factor of $s_f = 24$ (i.e., $a_{CC} = s_f a_0$ where $a_0 = 0.142 \text{ nm}$ is the well known C – C bond length in graphene) and simultaneously decreases the nearest neighbor hopping energy with the same factor (i.e., $t = t_0/s_f$ where $t_0 = 2.7 \text{ eV}$ is the typical tight-binding hopping energy [5]).

7 Anti-focusing with a constriction

In the main text, we study the appearance of low conductance spots (low G spots) in the experimental SGM maps. In order to understand the origin of these spots, we compare simulated SGM

maps (Fig. S6a) with current density maps simulated in a graphene sheet without constriction (Fig. S6b). In this section, we detail how to interpret the SGM map in relation to the current density map. In particular, we will explain why the low G spots (blue arrows in Fig. S6a) do not have exactly the same shape as the low current density spots (low \vec{J} spots, red arrows in Fig. S6b). Section 8 presents some perspectives towards getting a direct correspondence between the SGM maps and the current density around a p-n junction.

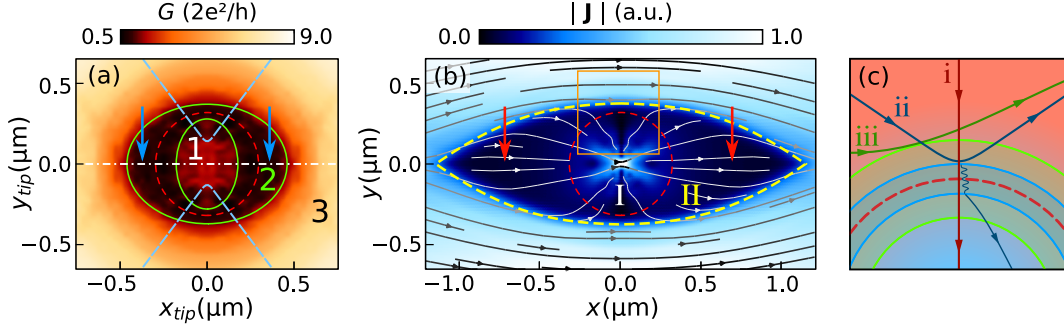


Figure S6: Comparison between simulated current density and SGM maps. (a-b) Same SGM maps as Fig. 4d and 4c in the main text. Different zones have been delimited on top of the maps for the discussion exposed in the text. Blue arrows indicate the position of the low G spots and red arrows indicate the position of the low \vec{J} spots. (c) Qualitative sketch illustrating the electron trajectories (i, ii and iii) impinging the circular smooth p-n junction in an area corresponding to the orange square in (b). A *forbidden zone* is associated to each trajectory (blue boundaries for trajectory ii and green for iii).

To properly understand the SGM maps, we performed simulations using our home-made code presented in section 6. Figure S7 shows simulations of the current density in a large graphene ribbon containing a constriction whose width is progressively lowered. The tip potential used in each figure is the same as in Fig. 4c-d of the main text. All the current density maps are normalised with the same factor J_{max} so they can be compared together.

Figure S7a shows a map of the current density in a ribbon without constriction that exhibits the two characteristic low \vec{J} spots. These spots are caused by the smooth p-n junction that bends the electrons trajectories. When the constriction width is lowered (Fig. S7b-e), the edges of the constriction also bend electrons trajectories towards the centre of the constriction. The conductance is therefore given by the combined influence of the tip potential and the constriction. The important feature observed in Fig. S7b-e is the reduction of the low \vec{J} spot size as the constriction width is lowered. This explains why the low G spots do not directly map the low \vec{J} spots.

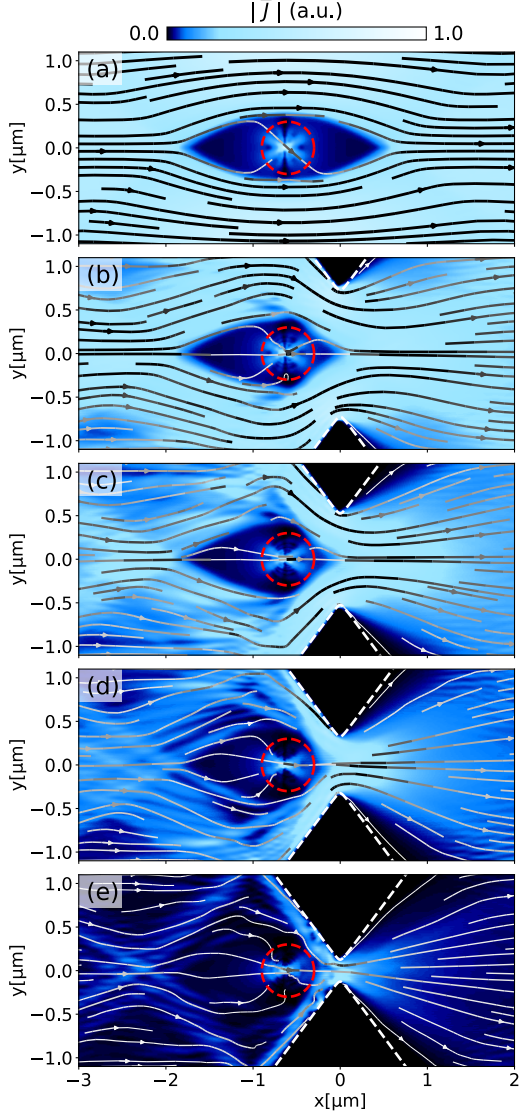


Figure S7: Simulation of current density when varying the constriction width. A Lorentzian potential ($V_m = 2E_F$) creates a circular p-n junction (red dashed line, $R_{tip} = 300$ nm). **(a)** Current density computed without constriction. Two spots of low current density appear, similarly to figure S6a. **(b-e)** Current density computed for constriction widths of respectively : **(b)** 1450 nm, **(c)** 1050 nm, **(d)** 650 nm and **(e)** 250 nm. The distance between the tip and the constriction is 600 nm.

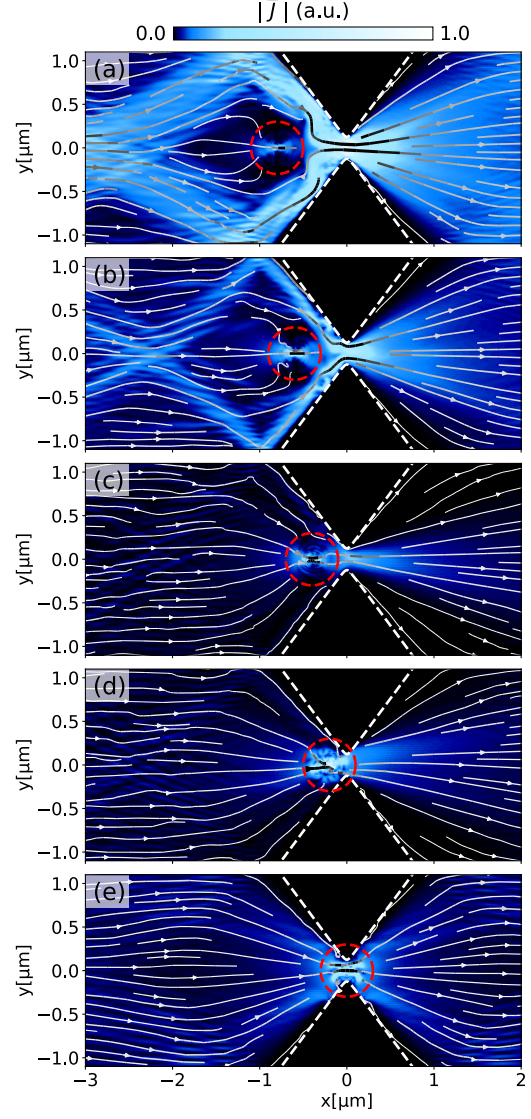


Figure S8: Simulation of current density when varying the tip position. A Lorentzian potential ($V_m = 2E_F$) creates a circular p-n junction (red dashed line, $R_{tip} = 300$ nm). The tip position is moved along x and is located at a distance from the constriction of **(a)** 800 nm **(b)** 600 nm, **(c)** 400 nm, **(d)** 200 nm and **(e)** 0 nm. The width of the constriction is 250 nm.

With the bending effect of the edges in mind, we can discuss the origin of the low G spots. Figure S8 illustrates the influence of the tip potential on the conductance for a constriction of 250 nm. The tip potential is the same as the one used in Fig. S7 and Fig. 4c-d. We can distinguish four situations:

1. When the tip is far from the centre of the constriction (Fig. S8a), electrons flow along the edges. The low \vec{J} spot at the constriction side disappears and the conductance remains high.
2. When the tip starts to get closer to the constriction (Fig. S8b), the trajectories along the edges encounter the p-n junction with a parallel incidence. Due to the junction smoothness, a *forbidden zone*¹ (illustrated in Fig. S6c) appears, whose width depends on the incident angle of the electron trajectories [8]. For parallel incidence (trajectory iii in Fig. S6c), the forbidden zone (delimited by green boundaries) is wide. By approaching the tip from the edge, the forbidden zone starts to block edge trajectories, reducing the conductance.
3. When further approaching the tip (Fig. S8c and d), the majority of trajectories will be blocked due to the effect of the forbidden zone around the p-n junction. Only the trajectories favoured by Klein tunnelling will go through the constriction. In this configuration, the transmission mainly depends on the constriction width and the p-n junction shape, as it will be illustrated in section 8.
4. Finally, when the tip is located at the centre of the constriction (Fig. S8e), the conductance is dominated by Klein tunnelling so that the transmission increases again. This is illustrated by trajectory i in Fig. S6c.

Since we have a good insight about the mechanisms at play when the tip approaches the constriction, we can summarise by establishing the correspondence between the SGM map of Fig. S6a and the current density map of Fig. S6b. To do so, the SGM map and the current density map have been divided into different zones in Fig. S6.

- **Zone 1** corresponds to an increase of the conductance. It is a direct consequence of the high current density in the lens core indicated by **zone I**. This region is therefore an image of Klein tunnelling in real space.
- **Zone 2** and **zone II** are a consequence of the smoothness of the junction. Zone 2 has its origin in the forbidden zone that blocks electron trajectories in the vicinity of the constriction, as discussed above in point 3. Zone II is also related to the presence of the forbidden zone. Indeed, only perpendicular trajectories cross the p-n junction. The smoothness of the potential also bends the trajectories, leading to the stretched shape of zone II along transport axis.
- **Zone 3** in Fig. S6a is given by potential positions that are far from the constriction center so that the perturbation has only a weak effect on the electron transmission.

Even if they are both due to the smoothness of the potential, zone 2 does not directly map zone II. Indeed, as highlighted in Fig. S7 and the related discussion, the bending of the electron trajectories, due to the constriction, suppresses the low \vec{J} spots. In section 8, we will see how the constriction geometry can be modified to map zone II in a SGM map.

¹By *forbidden zone*, we mean a zone that electrons can only cross by tunnelling (with a decaying exponential transmission), as illustrated by trajectory ii in Fig. S6c [8]

8 Constriction as a current density detector

In section 7, the origin of the low G spots in the SGM maps has been discussed. They are due to the effect of the smooth p-n interface that blocks the transmission of electrons when it is in the vicinity of the constriction. Due to the bending of the electron trajectories by the constriction edges, the low G spots do not have exactly the same shape as the low \vec{J} spots. In this section, we will detail how the design of the constriction can be modified in order to obtain a direct correspondence between the SGM map and the current density map without constriction. To do so, a constriction defined by vertical (i.e; perpendicular to the transport axis) boundaries is studied, as depicted in Fig. S9a. The constriction opening width, along y , is 250 nm and its length, along x , is 60 nm.

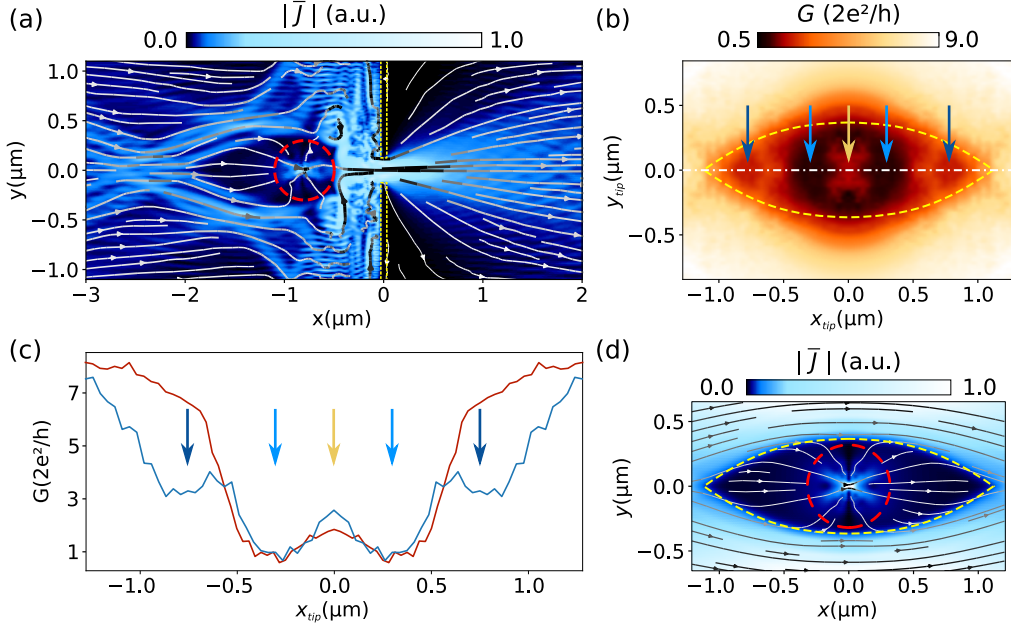


Figure S9: Effect of the constriction shape on the SGM maps. (a) Current density map in a constriction defined by vertical boundaries (yellow dashed line) in presence of a Lorentzian potential ($V_m = 2E_F$) that creates a circular p-n junction (red dashed line, $R_{tip} = 300$ nm). (b) SGM map in the same constriction and for the same Lorentzian potential as (a). The yellow dashed line shows the limits of the low current density zone shown in (d). (c) Blue curve: conductance at $y_{tip} = 0$, obtained along the white dash-dotted line of (b). Red curve: conductance curve at $y_{tip} = 0$, obtained along the white dash-dotted line of Fig. S6a. The arrows show three characteristic zones of the SGM map. (d) Same figure as Fig. S6 and Fig. 4c in the main text. The yellow dashed line delineates the low current density zone.

The SGM map obtained in the new constriction geometry is shown in Fig. S9b. It can be compared to the map of Fig. S6a obtained for the previous constriction geometry. Fig. S9c shows

line cuts at $y_{tip} = 0$ in the two SGM maps. The obtained conductance curves highlight the key differences between the two geometries. Three zones can be distinguished, indicated by arrows in Fig. S9b and c:

- The **gold arrow** indicates the zone of increased conductance caused by Klein tunnelling. This is the zone 1 discussed in section 7.
- **Light blue arrows** indicate the low G spots described by zone 2 in section 7. The position and the shape of these spots are rather similar for both constriction geometries, as highlighted in Fig. S9c. The shape of the low G spots therefore mainly depend on the constriction width and the effect of the p-n interface. The slope of the constriction boundaries will also slightly modify the shape. Indeed, the p-n interface will not reach the constriction edges at the same distance from the constriction center (see Fig. S8 and the related discussion - point 2). The conductance will therefore not fall at the same position, as illustrated in Fig. S9c.
- **Dark blue arrow** indicate plateaus of reduced conductance only visible for the vertical boundaries (blue curve in Fig. S9c). By comparing Fig. S9b and d, it appears that these zones of reduced conductance are directly related to the low \vec{j} . To emphasise this correspondence, the delimitation of the low \vec{j} zone (yellow dotted line in Fig. S9d) is reported on Fig. S9b.

The appearance of this last zone, for the vertical boundaries, can be explained by a less efficient bending of electron trajectories toward the center of the constriction, compared to the oblique edge (see section 7). Indeed, the vertical edges will mostly back-scatter electrons instead of bending their trajectories as illustrated by Fig. S9a (in comparison to Fig. S8). The low \vec{j} spots (zone III in Fig. S6) have therefore a real influence when the potential is in front of the constriction. This explains the good correspondence between Fig. S9b and d.

To conclude, the shape of the constriction plays an important role on the SGM data. By designing properly this constriction, it can be optimised to yield features that directly correspond to the current density around a tip-induced potential. This opens the way to new devices for SGM characterisation.

9 Turning off Klein tunneling and Veselago lensing

To get more clue about the role of graphene peculiar properties in our experiment, we modeled gapped graphene, by considering theoretically graphene aligned with a Boron-Nitride substrate. We induce a small gap compared to the energies in the p and n region, such that the local density of states is still high in both the p and n regions, as shown Fig. S10 f. This gap however prevents Klein tunneling and Veselago lensing effects. The effect on the current density is the disappearance of the high $|\vec{j}|$ region at the lens core (Fig. S10 g). Concomitantly, the spot of high conductance when placing the lens at the center of the constriction disappears in the case of gapped graphene, as visible by comparing the SGM images Fig. S10g (normal graphene) and S10h (gapped graphene).

This demonstrates that the SGM images indeed reflect the current density through the p-n junction, and not only the local density of states, or local conductivity. Though based on a different physical system, these calculations show that the perfect transmission between the p and n regions is crucial to obtain the effect observed experimentally. This high transmission is achieved thanks

to Klein tunneling, which is at play in our experiment, and appears as a necessary ingredient to understand the observed behavior.

It is however difficult to quantify the contributions from Veselago lensing and from Klein tunneling, as they're indeed different manifestations of the same phenomenon. The Veselago lensing effect denotes Klein tunneling at a finite incidence angle. In our experiment, the pn interface is circular, which offers a large variety of incident angles compared to planar interfaces used in previous experiments[9, 10]. By collecting different incident angles and refocusing them at the same point, our geometry therefore favors the effect of Veselago lensing compared to "normal" Klein tunneling.

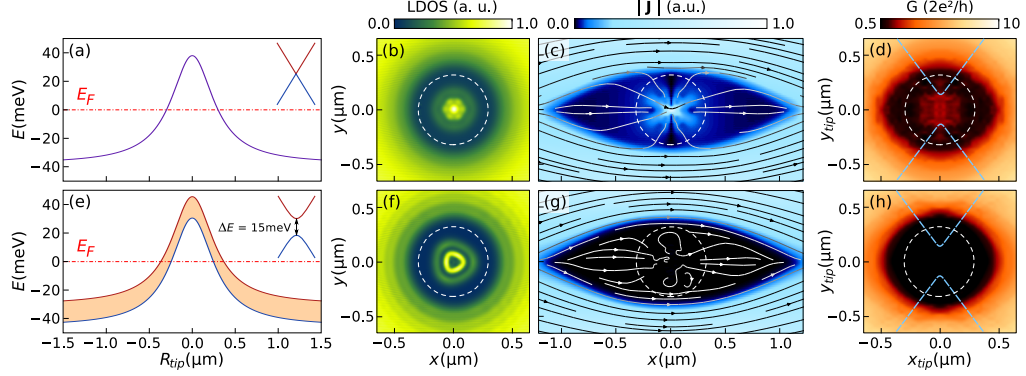


Figure S10: Turning off Klein tunneling with gapped graphene: (a) Potential profile used to calculate transport through graphene pn junction. (b) Local density of state (LDOS) for normal graphene in the circular pn junction. (c) Local current density for normal graphene. (d) SGM map expected when scanning the perturbation around a constriction. (e) Potential profile used in the case of gapped graphene. (f) LDOS for a gapped graphene p-n junction. (g) $|\vec{J}|$ in for gapped graphene. (h) SGM image computed for gapped graphene.

10 Effect of the junction smoothness

In this section, we present the current density and SGM maps for different decay exponent d of the tip-induced potential $V(\vec{r}) = \frac{V_m}{1 + \left(\frac{\|\vec{r} - \vec{r}_{tip}\|}{R_{tip}}\right)^d}$.

In Fig.S11, the effect of the junction smoothness on both the current density and the SGM maps is clarified. Fig.S11(c-f) correspond to the Lorentzian ($d=2$) and abrupt ($d=\infty$) potential profiles already presented in Fig.4 of the manuscript. Fig.S11g and h present the intermediate case of a potential that decays faster than a Lorentzian but still evolving smoothly ($d=5$). The distance of the anti-focusing points evolve in both the current density and the SGM maps. Finally, Fig.S11 a and b present \vec{J} and the SGM map in the n'-n configuration, where the density below the tip reaches the charge neutrality in a single point.

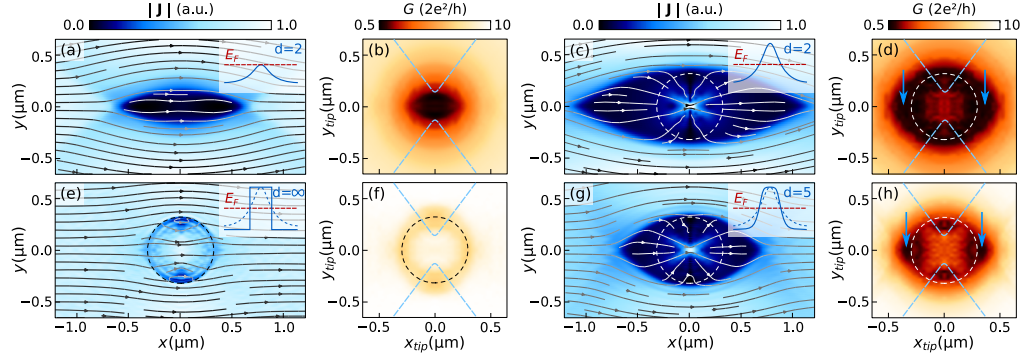


Figure S11: Influence of the junction smoothness: Simulations of current density \vec{j} in a graphene sheet around the fixed tip potential of Eq. (??) characterized by the parameters V_m , E and d (left image in each couple), and simulated SGM maps obtained by displacing the same potential around a 250 nm-wide constriction (right image in the couple). (a-b) Lorentzian profile ($d = 2$) with $V_m = E$. (c-d) n-p-n configuration with $d = 2$ and $V_m = 2E$. (e-f) Abrupt circular p-n junction with $d = \infty$ and $V_m = 2E$. (g-h) Fast decaying potential profile ($d = 5$) with $V_m = 2E$. The chosen energy E corresponds in all cases to $n = 1.5 \times 10^{15} \text{m}^{-2}$, and $\Delta n_{max} = -3 \times 10^{15} \text{m}^{-2}$ in (c) to (h). Dashed circle indicates the *locus* corresponding to zero charge density. Insets: schematics of potential profile vs position, Lorentzian profile is indicated as dashed blue line for comparison, when $d \neq 2$.

11 Fabry-Pérot interference

In Fig.S12(a), we plot the conductance as a function of V_{tip} of V_{bg} , recorded at 4K by placing the tip at the center of the constriction, 70 nm above the sample surface. Clear oscillations are visible in the n-p-n and p-n-p configurations, due to Fabry-Pérot interference. The series ohmic contact resistance peak is visible at $V_{bg} \simeq 2.5$ V and is insensitive to tip voltage since this contact is situated far away from the constriction. It can hence clearly be distinguished from the Fabry-Pérot interferences. These interferences are at the moment under deeper investigation and will be detailed in another paper.

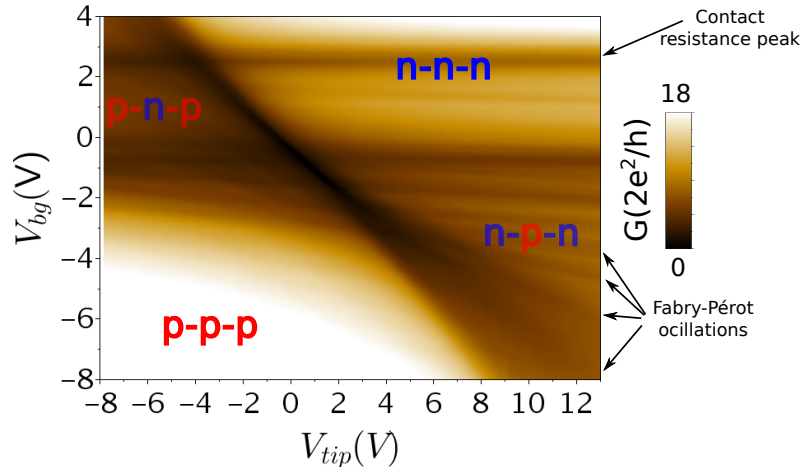


Figure S12: Fabry-Pérot interference: Conductance G as a function of tip voltage V_{tip} and back-gate voltage V_{bg} , when placing the tip at the center of the constriction, at a distance $d_{tip} = 70$ nm from the sample surface.

References

- [1] K. K. Kim *et al.*, *Synthesis and characterization of hexagonal boron nitride film as a dielectric layer for graphene devices*, ACS Nano **6**, 8583 (2012)
- [2] B. Huard *et al.*, *Transport Measurements Across a Tunable Potential Barrier in Graphene*, Phys. Rev. Lett. **98**, 236803 (2007)
- [3] V. H. Nguyen *et al.*, *Bandgap nanoengineering of graphene tunnel diodes and tunnel transistors to control the negative differential resistance*, J. Comput. Electron. **12**, 85 (2013)
- [4] C. W. Groth *et al.*, *Kwant: a software package for quantum transport*, New J. Phys **16**, 063065 (2014)
- [5] A. H. Castro Neto *et al.*, *The electronic properties of graphene*, Rev. Mod. Phys. **81**, 109 (2009)
- [6] C. H. Lewenkopf *et al.*, *The recursive green's function method for graphene*, J. Comput. Electron. **12**, 203 (2013)
- [7] M.-H. Liu *et al.*, *Scalable tight-binding model for graphene*, Phys. Rev. Lett. **114**, 036601 (2015)
- [8] V. V. Cheianov and V. I. Fal'ko, *Selective transmission of Dirac electrons and ballistic magnetoresistance of n-p junctions in graphene*, Phys. Rev. B **74**, 041403(R) (2006)
- [9] G.-H. Lee, G.-H. Park, and H.-J. Lee, *Observation of negative refraction of Dirac fermions in graphene*, Nature Physics **11**, 925 (2015).
- [10] S. Chen *et al.*, *Electron optics with p-n junctions in ballistic graphene*, Science **353**, 1522 (2016).